A Complex View of Barycentric Mappings

O. Weber[1]   M. Ben-Chen[2]   C. Gotsman[3]   K. Hormann[4]

[1]Courant Institute of Mathematical Sciences, New York University, USA
[2]Computer Science Department, Stanford University, USA
[3]Computer Science Department, Technion, Haifa, Israel & Department of Computer Science, ETH Zürich, Switzerland
[4]Faculty of Informatics, University of Lugano, Switzerland

Abstract

Barycentric coordinates are very popular for interpolating data values on polyhedral domains. It has been recently shown that expressing them as complex functions has various advantages when interpolating two-dimensional data in the plane, and in particular for holomorphic maps. We extend and generalize these results by investigating the complex representation of real-valued barycentric coordinates, when applied to planar domains. We show how the construction for generating real-valued barycentric coordinates from a given weight function can be applied to generating complex-valued coordinates, thus deriving complex expressions for the classical barycentric coordinates: Wachspress, mean value, and discrete harmonic. Furthermore, we show that a complex barycentric map admits the intuitive interpretation as a complex-weighted combination of edge-to-edge similarity transformations, allowing the design of "home-made" barycentric maps with desirable properties. Thus, using the tools of complex analysis, we provide a methodology for analyzing existing barycentric mappings, as well as designing new ones.

Categories and Subject Descriptors (according to ACM CCS): I.3.3 [Computer Graphics]: Picture/Image Generation—Line and curve generation; G.1.1 [Numerical Analysis]: Interpolation—Interpolation formulas

1. Introduction

Barycentric coordinates have become very popular over recent years for interpolating data values f_j that are given at the vertices $v_j = (x_j, y_j)$, $j = 1, \ldots, n$ of a planar polygon $\Omega \subset \mathbb{R}^2$. A set of functions $b_j \colon \Omega \to \mathbb{R}$, $j = 1, \ldots, n$ is called a set of *barycentric coordinates* or *barycentric basis functions* if the b_j have *affine precision*, that is,

$$\sum_{j=1}^{n} b_j(v)\phi(v_j) = \phi(v) \qquad (1)$$

for any point $v = (x, y)$ inside Ω and any affine function $\phi(x, y) = \alpha x + \beta y + \gamma$ with $\alpha, \beta, \gamma \in \mathbb{R}^d$. This property is often split into two equivalent properties: that the barycentric coordinates form a *partition of unity*,

$$\sum_{j=1}^{n} b_j(v) = 1, \qquad (2)$$

and that any $v \in \Omega$ can be written as an *affine combination* of the polygon's vertices,

$$\sum_{j=1}^{n} b_j(v)v_j = v. \qquad (3)$$

The idea now is to use the weights $b_j(v)$ of this affine combination for blending the data values f_j and to define the function f over Ω as

$$f(v) = \sum_{j=1}^{n} b_j(v)f_j. \qquad (4)$$

If the barycentric coordinates further satisfy the *Lagrange interpolation property*

$$b_j(v_k) = \delta_{jk} = \begin{cases} 1, & \text{if } j = k, \\ 0, & \text{if } j \neq k, \end{cases}$$

then it is clear that f interpolates the given data f_j at the vertices v_j. Another, sometimes desirable property is the *non-negativity* of the barycentric coordinates,

$$b_j(v) \geq 0$$

for $v \in \Omega$, which guarantees that the function values $f(v)$ are contained in the convex hull of the data values f_j.

The interpolant f in (4) is particularly appealing for applications if the b_j are given in closed form. Over the past few years, a number of recipes for such closed-form barycentric coordinates have been developed. Probably the most
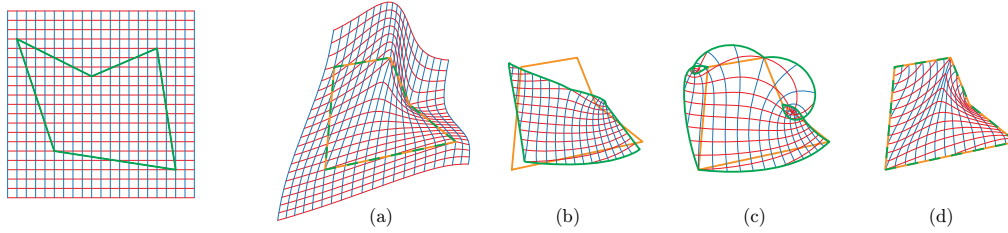
Figure 1: *A barycentric mapping is defined by a source polygon (green), a target polygon (orange), and some choice of barycentric coordinates, whose properties are inherited by the mapping. The mapping based on real-valued mean value coordinates (a) linearly interpolates the edges of the target polygon, is well-defined in the entire plane, but considerably distorts local areas and angles. The complex Cauchy–Green mapping (b) does not even interpolate the target vertices, is defined only in the interior of the source polygon, but preserves angles. It is also possible to design complex angle-preserving mappings that interpolate the target vertices (see Section 4.2), albeit at the price of singularities and fold-overs (c). Interpolation of the entire target polygon by a truly complex mapping (d) can be achieved by compromising the angle-preservation (see Section 4.3).*

well-known are the discrete harmonic (also called cotangent weights) [PP93, EDD*95], mean value [Flo03, HF06], and Wachspress [Wac75, MLBD02] coordinates. Floater et al. [FHK06] show that all three are just special cases of a general family of *three-point coordinates* (see Section 2), and Ju et al. [JLW07] extend their construction to higher dimensions. While discrete harmonic and Wachspress coordinates are well-defined only inside convex polygons, mean value coordinates are well-defined for arbitrary simple polygons [HF06], but they are not necessarily non-negative. Positive mean value coordinates [LKCOL07] overcome this limitation at the cost of being only C^0-continuous. The only known smooth barycentric coordinates that are non-negative even for arbitrary simple polygons are the harmonic [JMD*07] and maximum entropy coordinates [HS08], but both do not have a closed form and can only be approximated numerically. All these coordinates satisfy the Lagrange property and are piecewise linear along the boundary $\partial\Omega$ of the polygon.

1.1. Barycentric mappings

While originally designed for interpolating scalar data, it is also possible to apply the same methodology to vector data. In particular, if the data f_j is two-dimensional, then f in (4) may be viewed as a mapping from the plane to itself. This setting has important applications in two-dimensional computer graphics, in particular for image and shape deformation. In this scenario we have two planar polygons (see Figure 1), a *source polygon* Ω with *source vertices* v_j and a corresponding *target polygon* $\hat{\Omega}$ with the same number of *target vertices* $\hat{v}_j$, and we are interested in the *barycentric mapping*

$$f(v) = \sum_{j=1}^{n} b_j(v)\hat{v}_j. \qquad (5)$$

If we use any of the barycentric coordinates mentioned above, then the boundary of the source polygon is mapped to

the boundary of the target polygon, $f(\partial\Omega) = \partial\hat{\Omega}$, due to the piecewise linear behaviour of the b_j along $\partial\Omega$. Moreover, if the target vertices are the image of an affine transformation $\phi : \mathbb{R}^2 \to \mathbb{R}^2$, that is, $\hat{v}_j = \phi(v_j)$, $j = 1, \ldots, n$, then it follows from (1) that $f = \phi$. Although this might be perceived as an advantage, affine precision is not very natural in the planar deformation scenario, because affine stretches and shears produce deformations which do not preserve small details.

To rectify this, Lipman et al. [LLCO08] and Weber et al. [WBCG09] introduce the so-called Cauchy–Green coordinates, which reproduce conformal mappings. To achieve this, they depart from the classical barycentric coordinate scenario by abandoning the Lagrange interpolation property, and so the images of the source vertices $f(v_j)$ may no longer coincide with the target vertices $\hat{v}_j$; see Figure 1 (b). The construction of these coordinates relies on the Cauchy integral formula from complex analysis, or the somewhat equivalent Green's third identity from vector analysis. Weber et al. [WBCG09] further demonstrate that using complex numbers significantly simplifies the formulation of the barycentric mappings based on Cauchy–Green coordinates and the proofs of related theorems.

In the complex setting, we interpret the source polygon Ω as a subset of $\mathbb{C}$ and represent its vertices $v_j = (x_j, y_j)$ as complex numbers $z_j = x_j + iy_j$, and similarly for the target polygon. In analogy to properties (2) and (3), a set of functions $c_j : \Omega \to \mathbb{C}$, $j = 1, \ldots, n$ is then called a set of *complex barycentric coordinates*, if

$$\sum_{j=1}^{n} c_j(z) = 1 \qquad (6)$$

and

$$\sum_{j=1}^{n} c_j(z)z_j = z \qquad (7)$$

for any complex number $z = x + iy$ that represents a point $v = (x, y)$ inside Ω.

As in the real setting, these conditions are equivalent to the affine precision property, hence the *complex barycentric mapping*

$$g(z) = \sum_{j=1}^{n} c_j(z)\hat{z}_j \qquad (8)$$

reproduces *complex affine functions* $\psi(z) = \alpha z + \beta$ with $\alpha, \beta \in \mathbb{C}$. It is important to note that complex affine functions $\psi \colon \mathbb{C} \to \mathbb{C}$ are less general than affine transformations $\phi \colon \mathbb{R}^2 \to \mathbb{R}^2$. In fact, they capture only the subset of similarity transformations, but in the context of image and shape deformation this restriction is an advantage. Unlike their bivariate real-valued siblings, complex barycentric mappings do not necessarily reproduce visually disturbing shears and non-uniform stretches, and thus provide more control for the design of favourable deformations.

1.2. Contributions

The goal of this paper is an in-depth study of the structure and properties of complex barycentric mappings. We first present some geometric insight into the general construction of barycentric coordinates and show how the classical real-valued coordinates (Wachspress, mean value, and discrete harmonic) can be interpreted as a family of complex-valued coordinates (Section 2). We then discuss the expressive power of complex-weighted barycentric maps, showing in which cases the complex formulation is more flexible (Section 3). Using this new flexibility and the insights into the various components which affect the behaviour of the map, we give a few examples of new mappings, demonstrating the design considerations involved in hand-crafting complex maps (Section 4). These examples also showcase the true power of complex coordinates: the ability to "mix" the *x* and *y* coordinates, instead of treating them separately as maps based on real-valued coordinates do. Combined together, our results provide an extensive toolbox for analysis and design of both real-valued and complex-valued barycentric mappings.

2. From real-valued to complex-valued coordinates

It is natural to ask whether the traditional real-valued coordinates can be expressed in some natural complex form. Of course, any real number is also a complex number and thus real-valued coordinates are by definition also complex-valued coordinates. However, it has been shown that a general construction exists, both in the real and the complex case, which transforms arbitrary "weight functions" to barycentric coordinates. These weight functions are sometimes more useful for analyzing the behaviour of the coordinates than the coordinates themselves, thus we wish to relate real- and complex-valued coordinates in terms of these weight functions.
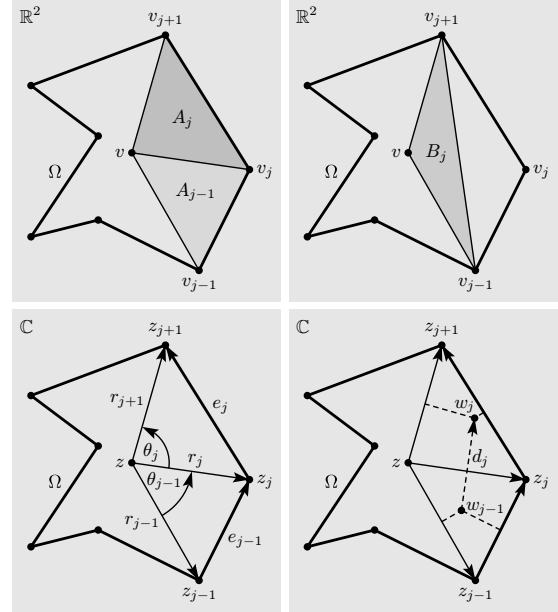

Figure 2: *Notation used in the real (top) and the complex setting (bottom).*

2.1. The normal form of barycentric coordinates

First, consider the result of Floater et al. [FHK06, Corollary 3] that any set of barycentric coordinates b_j can be written in the form

$$b_j = \frac{\tilde{b}_j}{\sum_{k=1}^{n} \tilde{b}_k}, \qquad \tilde{b}_j = \frac{\beta_{j+1} A_{j-1} - \beta_j B_j + \beta_{j-1} A_j}{A_{j-1} A_j} \quad (9)$$

for certain "weight functions" $\beta_j \colon \Omega \to \mathbb{R}$, where $A_j(v)$ and $B_j(v)$ are the signed areas of the triangles $[v, v_j, v_{j+1}]$ and $[v, v_{j-1}, v_{j+1}]$, respectively (see Figure 2), with indices taken cyclically over the valid range $1, \dots, n$. Moreover, the b_j in (9) constitute a set of barycentric coordinates for any choice of functions β_j [FHK06, Proposition 5], as long as the denominator $\sum_{j=1}^{n} \tilde{b}_j(z)$ does not vanish.

Similarly, Weber et al. [WBCG09, Theorem 5] remark that any set of complex barycentric coordinates c_j can be expressed in the form

$$c_j = \frac{\tilde{c}_j}{\sum_{k=1}^{n} \tilde{c}_k}, \qquad \tilde{c}_j = \gamma_j \frac{r_{j+1}}{e_j} - \gamma_{j-1} \frac{r_{j-1}}{e_{j-1}} \quad (10)$$

for certain weight functions $\gamma_j \colon \Omega \to \mathbb{C}$, where $r_j(z) = z_j - z$ and $e_j = z_{j+1} - z_j$ (see Figure 2). Conversely, any choice of functions γ_j in (10) gives a set of complex barycentric coordinates c_j [WBCG09, Theorem 4], provided that $\sum_{j=1}^{n} \tilde{c}_j(z) \neq 0$, which is actually equivalent to the condition $\sum_{j=1}^{n} \gamma_j(z) \neq 0$ (see Section 3).

This justifies one to refer to the forms (9) and (10) as the *normal form* of real and complex barycentric coordinates, respectively.

Both constructions are closely related to the defining properties of barycentric coordinates. In fact, the normalization from homogeneous coordinates $\tilde{b} = (\tilde{b}_1, \ldots, \tilde{b}_n)$ to normalized coordinates $b = (b_1, \ldots, b_n)$ in (9) takes care of the latter forming a partition of unity (2), and the linear transformation $B \colon \mathbb{R}^n \to \mathbb{R}^n$ in (9), that maps the weights $\beta = (\beta_1, \ldots, \beta_n)$ to $\tilde{b} = (\tilde{b}_1, \ldots, \tilde{b}_n)$, guarantees that

$$\sum_{j=1}^{n} \tilde{b}_j(v)(v_j - v) = 0,$$

which, together with partition of unity, yields the affine combination property (3). Geometrically, this means that B maps into the $(n-2)$-dimensional linear subspace of $\mathbb{R}^n$ that is orthogonal to the two vectors $(x_1 - x, \ldots, x_n - x)$ and $(y_1 - y, \ldots, y_n - y)$, hence the kernel of B is 2-dimensional. The normalization further reduces the dimension by one, and so the (non-linear) space of real-valued barycentric coordinates for any point $v \in \Omega$ is $(n-3)$-dimensional.

For complex-valued coordinates, the two transformations in (10) correspond analogously to the defining properties (6) and (7). The only difference is that the kernel of the linear transformation $C \colon \mathbb{C}^n \to \mathbb{C}^n$, which maps the weights $\gamma = (\gamma_1, \ldots, \gamma_n)$ to homogeneous coordinates $\tilde{c} = (\tilde{c}_1, \ldots, \tilde{c}_n)$ and guarantees that

$$\sum_{j=1}^{n} \tilde{c}_j(v)(z_j - z) = 0,$$

is only 1-dimensional (essentially, the two real dimensions of $\ker(B)$ are combined into one complex dimension). Therefore, the (non-linear) space of complex-valued barycentric coordinates for any $z \in \Omega$ is $(n-2)$-dimensional, and unlike in the real setting, they are not unique if Ω is a triangle. It is easy to verify that the kernel of C is spanned by the vector

$$\bar{\gamma} = (\bar{\gamma}_1, \ldots, \bar{\gamma}_n) \qquad \text{with} \qquad \bar{\gamma}_j = \frac{e_j}{r_j r_{j+1}}, \qquad (11)$$

hence adding any multiple of $\bar{\gamma}$ to γ does not change the corresponding complex coordinates $c = (c_1, \ldots, c_n)$.

2.2. The complex form of real-valued coordinates

We are now ready to relate the two normal forms.

Theorem 1 For any set of real-valued barycentric coordinates b_j, $j = 1, \ldots, n$, let β_j be the weight functions from their representation in (9) and define

$$\gamma_j = \frac{e_j}{\operatorname{Im}(\bar{r}_j r_{j+1})} \left(\frac{\beta_{j+1}}{r_{j+1}} - \frac{\beta_j}{r_j} \right). \qquad (12)$$

Then the corresponding complex barycentric coordinates c_j in (10) are equivalent to b_j, in the sense that $\operatorname{Re}(c_j) = b_j$ and $\operatorname{Im}(c_j) = 0$.

Proof Using the representations $\bar{r}_j = (x_j - x) - i(y_j - y)$ and $r_{j+1} = (x_{j+1} - x) + i(y_{j+1} - y)$, we have

$$\operatorname{Im}(\bar{r}_j r_{j+1}) = \left[(x_j - x)(y_{j+1} - y) - (x_{j+1} - x)(y_j - y) \right],$$

hence

$$\operatorname{Im}(\bar{r}_j r_{j+1}) = \begin{vmatrix} x_j - x & x_{j+1} - x \\ y_j - y & y_{j+1} - y \end{vmatrix} = 2A_j,$$

and similarly

$$\operatorname{Im}(\bar{r}_{j-1} r_{j+1}) = 2B_j.$$

Substituting (12) into (10) gives

$$2\tilde{c}_j = \frac{e_j}{A_j} \left(\frac{\beta_{j+1}}{r_{j+1}} - \frac{\beta_j}{r_j} \right) \frac{r_{j+1}}{e_j} - \frac{e_{j-1}}{A_{j-1}} \left(\frac{\beta_j}{r_j} - \frac{\beta_{j-1}}{r_{j-1}} \right) \frac{r_{j-1}}{e_{j-1}}$$

$$= \frac{\beta_{j+1}}{A_j} - \frac{\beta_j}{r_j} \left(\frac{r_{j+1}}{A_j} + \frac{r_{j-1}}{A_{j-1}} \right) + \frac{\beta_{j-1}}{A_{j-1}}$$

$$= \frac{\beta_{j+1}}{A_j} - \frac{\beta_j}{A_{j-1} A_j} B_j + \frac{\beta_{j-1}}{A_{j-1}},$$

where we used the identity $r_{j+1} A_{j-1} + r_{j-1} A_j = r_j B_j$ in the last step, which in turn follows from the well-known fact that

$$\alpha_1 \operatorname{Im}(\alpha_2 \bar{\alpha}_3) + \alpha_2 \operatorname{Im}(\alpha_3 \bar{\alpha}_1) + \alpha_3 \operatorname{Im}(\alpha_1 \bar{\alpha}_2) = 0$$

for any $\alpha_1, \alpha_2, \alpha_3 \in \mathbb{C}$. The functions $\tilde{c}_j$ are therefore equivalent to the functions $\tilde{b}_j / 2$, and the factor $1/2$ is cancelled out by the normalization. $\quad\square$

Another justification for the normal form in (9) is that the Wachspress, mean value, and discrete harmonic coordinates are given by the simple choice $\beta_j(v) = \|v_j - v\|^p$ with $p = 0$, $p = 1$, and $p = 2$, respectively. Hence, the complex normal form of these coordinates follows immediately from Theorem 1.

Corollary 2 The complex normal form (10) of Wachspress, mean value, and discrete harmonic coordinates is given by the weight functions

$$\gamma_j = \frac{e_j}{\operatorname{Im}(\bar{r}_j r_{j+1})} \left(\frac{|r_{j+1}|^p}{r_{j+1}} - \frac{|r_j|^p}{r_j} \right) \qquad (13)$$

with $p = 0$, $p = 1$, and $p = 2$, respectively.

It is interesting to check in which cases these weight functions are real-valued. For $p = 2$ this is the case because γ_j simplifies to

$$\gamma_j = \frac{e_j(\bar{r}_{j+1} - \bar{r}_j)}{\operatorname{Im}(\bar{r}_j r_{j+1})} = \frac{|e_j|^2}{2A_j},$$

using the fact that $\alpha\bar{\alpha} = |\alpha|^2$ for any $\alpha \in \mathbb{C}$. This also yields a nice geometric interpretation of the discrete harmonic weight functions as the "aspect ratio" of the triangle $[z, z_j, z_{j+1}]$, namely the ratio between the length $|e_j|$ of its base $[z_j, z_{j+1}]$ and its height $h_j = 2A_j/|e_j|$.

For general p we can rewrite γ_j in (13) as

$$\gamma_j = \frac{r_{j+1} - r_j}{\operatorname{Im}(\bar{r}_j r_{j+1})} \left(\frac{|r_{j+1}|^p}{r_{j+1}} - \frac{|r_j|^p}{r_j} \right) =$$

$$= \frac{|r_{j+1}|^p - r_j \bar{r}_{j+1} |r_{j+1}|^{p-2} - r_{j+1} \bar{r}_j |r_j|^{p-2} + |r_j|^p}{\operatorname{Im}(\bar{r}_j r_{j+1})}$$
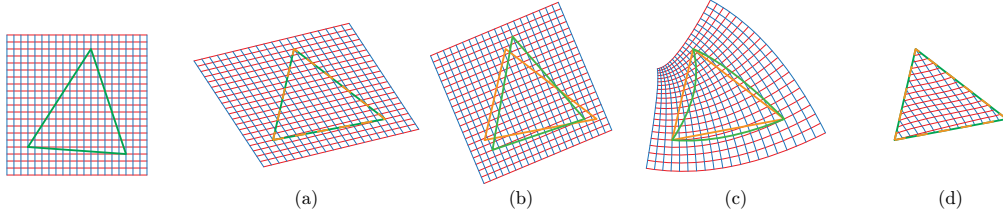
Figure 3: *Barycentric mappings from the green source triangle to the orange target triangle: unique real mapping (a), complex mappings for $\gamma_j = 1$, a global similarity (b) and $\gamma_j = r_{j+1}/r_j - r_j/r_{j+1}$, an angle-preserving vertex interpolant (c), and the complex mapping from Section 4.3 (d).*

and notice that the first and last term are purely real. Applying the simple identities

$$\text{Im}\left(\frac{z}{\text{Im}(z)}\right) = 1, \qquad \text{Im}\left(\frac{\bar{z}}{\text{Im}(z)}\right) = -1$$

to the second and third term, we find that

$$\text{Im}(\gamma_j) = |r_{j+1}|^{p-2} - |r_j|^{p-2},$$

and conclude that γ_j is real-valued if and only if $p = 2$.

In fact, it turns out that the discrete harmonic coordinates are the *only* real-valued barycentric coordinates among *all* possible constructions (that is, beyond the three-point family considered in Corollary 2) with a real-valued weight function γ_j in the complex normal form, as the following theorem shows.

Theorem 3 The weight functions γ_j in (12) are all real-valued if and only if the weight functions β_j are all of the form $\beta_j = \lambda |r_j|^2$ for some $\lambda \in \mathbb{R}$.

Proof The same line of argument as above shows that

$$\text{Im}(\gamma_j) = \frac{\beta_{j+1}}{|r_{j+1}|^2} - \frac{\beta_j}{|r_j|^2}$$

for the weight functions γ_j in (12). Thus, they are all real-valued if and only if the vector $(\beta_1, \ldots, \beta_n)$ lies in the null space of the matrix

$$G = \begin{pmatrix} |r_1|^{-2} & -|r_2|^{-2} & 0 & \ldots & 0 \\ 0 & |r_2|^{-2} & -|r_3|^{-2} & \ldots & 0 \\ & \ddots & \ddots & \ddots & \\ 0 & \ldots & 0 & |r_{n-1}|^{-2} & -|r_n|^{-2} \\ -|r_1|^{-2} & 0 & \ldots & 0 & |r_n|^{-2} \end{pmatrix}.$$

Multiplying G from the right with the diagonal matrix $D = \text{diag}\left(|r_1|^2, |r_2|^2, \ldots, |r_n|^2\right)$, we get the matrix

$$G \cdot D = \begin{pmatrix} 1 & -1 & 0 & \ldots & 0 \\ 0 & 1 & -1 & \ldots & 0 \\ & \ddots & \ddots & \ddots & \\ 0 & \ldots & 0 & 1 & -1 \\ -1 & 0 & \ldots & 0 & 1 \end{pmatrix},$$

whose null space is spanned by $(1, 1, \ldots, 1)$. The theorem then follows from the fact that x is in the null space of G if and only if $D^{-1}x$ is in the null space of $G \cdot D$. $\square$

3. The expressive power of complex barycentric maps

One of the consequences of Theorem 1 is that any real barycentric mapping f in (5) can also be expressed as a complex barycentric mapping g in (8). If we further consider the simple case of a barycentric mapping between two triangles, then it is clear that the set of complex barycentric mappings is a proper superset of the set of real barycentric mappings. Due to the affine precision property, all real barycentric maps are equal to the unique affine transformation from source to target triangle in this case, but complex barycentric maps are more flexible, even in this simple setting (see Figure 3).

In fact, it turns out that *any* complex function $h: \mathbb{C} \to \mathbb{C}$ can be written in complex barycentric form under very mild assumptions. To see this, we first reconsider the complex normal form in (10) and observe that

$$\sum_{j=1}^{n} \tilde{c}_j = \sum_{j=1}^{n} \gamma_j \frac{r_{j+1}}{e_j} - \sum_{j=1}^{n} \gamma_{j-1} \frac{r_{j-1}}{e_{j-1}}$$
$$= \sum_{j=1}^{n} \gamma_j \frac{r_{j+1}}{e_j} - \sum_{j=1}^{n} \gamma_j \frac{r_j}{e_j} = \sum_{j=1}^{n} \gamma_j \frac{r_{j+1} - r_j}{e_j} = \sum_{j=1}^{n} \gamma_j,$$

hence

$$\sum_{j=1}^{n} c_j \hat{z}_j = \left(\sum_{j=1}^{n} \gamma_j \frac{r_{j+1}}{e_j} \hat{z}_j - \sum_{j=1}^{n} \gamma_{j-1} \frac{r_{j-1}}{e_{j-1}} \hat{z}_j\right) \Big/ \sum_{j=1}^{n} \tilde{c}_j$$
$$= \sum_{j=1}^{n} \gamma_j \frac{r_{j+1}\hat{z}_j - r_j\hat{z}_{j+1}}{e_j} \Big/ \sum_{j=1}^{n} \gamma_j.$$

Now introducing for $j = 1, \ldots, n$ the similarity transformation

$$s_j(z) = \frac{r_{j+1}(z)\hat{z}_j - r_j(z)\hat{z}_{j+1}}{e_j},$$

which linearly maps the source edge $[z_j, z_{j+1}]$ to the corresponding target edge $[\hat{z}_j, \hat{z}_{j+1}]$, leads to the *normal form* of

complex barycentric mappings,

$$g(z) = \sum_{j=1}^{n} \gamma_j(z) s_j(z) \Big/ \sum_{j=1}^{n} \gamma_j(z). \qquad (14)$$

Thus, any complex barycentric mapping is a (normalized) blending of the linear edge-to-edge mappings s_j. Conversely, any choice of weight functions γ_j in (14) gives a complex barycentric mapping. However, care should be taken to avoid a vanishing denominator $\Gamma(z) = \sum_{j=1}^{n} \gamma_j(z)$, at least for all $z \in \Omega$ or even all $z \in \mathbb{C}$, so that the mapping is guaranteed to be well-defined. In particular, the weight vector $\gamma = (\gamma_1, \ldots, \gamma_n)$ must not be a multiple of $\bar{\gamma}$ in (11). A simple choice that guarantees $\Gamma(z) \neq 0$ is to set $\gamma_j(z) = 1$ for all j, but the resulting global similarity $g(z) = \sum_{j=1}^{n} s_j(z)/n$ does not satisfy any interpolation constraints, see Figure 3 (b).

We are now ready to state the full expressive power of complex barycentric mappings.

Theorem 4 Any complex function $h : \mathbb{C} \to \mathbb{C}$ can be written as a complex barycentric mapping, as long as source and target polygon are not similar to each other.

Proof First assume that Ω and $\hat{\Omega}$ are not similar to each other. Then there exists some index j such that the two similarity transforms s_{j-1} and s_j are not the same. Letting $\gamma_{j-1} = s_j - h$, $\gamma_j = h - s_{j-1}$, and $\gamma_k = 0$ for $k \neq j-1, j$ in (14) then gives

$$g = \frac{(s_j - h)s_{j-1} + (h - s_{j-1})s_j}{(s_j - h) + (h - s_{j-1})} = \frac{h(-s_{j-1} + s_j)}{s_j - s_{j-1}} = h,$$

for any complex function h.

However, if Ω and $\hat{\Omega}$ are similar to each other, then all s_j are the same and the previous construction is not possible. In fact, it follows from the reproduction property of complex barycentric mappings that g is the unique complex affine function that maps z_j to $\hat{z}_j$ for all $j = 1, \ldots, n$. Hence, for any other complex function h it is impossible to express it as a barycentric mapping in this situation. $\square$

Of course, the statement of Theorem 4 is purely theoretical, because the coordinates depend on the target polygon, and more importantly, because in practical applications we do not want to reproduce a specific complex function but rather aim for a general and simple choice of weight functions γ_j that provides favourable barycentric mappings.

3.1. Interpolation conditions

The key to choosing weight functions γ_j is understanding the influence that various properties of γ_j have on the resulting mapping. For example, since the similarities s_j are holomorphic functions, g is holomorphic if the γ_j are holomorphic, too. This is the case for the Cauchy–Green coordinates [WBCG09], where $\gamma_j = \log(r_{j+1}/r_j)$.

Another desirable property is the interpolation of the target polygon. While real-valued barycentric maps usually

have this feature built-in, the known complex-valued mappings [WBCG09, WG10] generally do not even interpolate the target vertices. Hence, when designing new complex mappings, the following sufficient conditions on the weight functions γ_j can be helpful.

Theorem 5 The complex barycentric mapping g in (14) interpolates the j-th target vertex, if

(1) $\lim_{z \to z_j} |\gamma_{j-1}(z) + \gamma_j(z)| = \infty,$

(2) $\lim_{z \to z_j} |\gamma_k(z) r_j(z)| < \infty, \qquad k = j-1, j,$

(3) $\lim_{z \to z_j} |\gamma_k(z)| < \infty, \qquad k \neq j-1, j.$

Proof It follows directly from the third condition that $\lim_{z \to z_j} \tilde{c}_k(z)$ is finite for $k \neq j-1, j, j+1$, so let us focus on the remaining three cases. For $k = j-1$ we have

$$\lim_{z \to z_j} \tilde{c}_{j-1}(z) = \lim_{z \to z_j} \left(\gamma_{j-1}(z) \frac{r_j(z)}{e_{j-1}} - \gamma_{j-2}(z) \frac{r_{j-2}(z)}{e_{j-2}} \right)$$
$$= \frac{1}{e_{j-1}} \lim_{z \to z_j} \gamma_{j-1}(z) r_j(z) - \frac{z_{j-2} - z_j}{e_{j-2}} \lim_{z \to z_j} \gamma_{j-2}(z),$$

which is finite due to the second and third condition, and similarly for $k = j+1$. Finally, by the first condition,

$$\lim_{z \to z_j} |\tilde{c}_j(z)| = \lim_{z \to z_j} \left| \gamma_j(z) \frac{z_{j+1} - z}{e_j} - \gamma_{j-1}(z) \frac{z_{j-1} - z}{e_{j-1}} \right|$$
$$= \lim_{z \to z_j} |\gamma_j(z) + \gamma_{j-1}(z)| = \infty.$$

As in the real case, this yields $\lim_{z \to z_j} \tilde{c}_k(z)/\tilde{c}_j(z) = \delta_{jk}$ (see e.g. [ZS08, Chapter 2.6]), so

$$\lim_{z \to z_j} c_k(z) = \lim_{z \to z_j} \frac{\tilde{c}_k(z)}{\sum_{l=1}^{n} \tilde{c}_l(z)} = \lim_{z \to z_j} \frac{\tilde{c}_k(z)/\tilde{c}_j(z)}{\sum_{l=1}^{n} \tilde{c}_l(z)/\tilde{c}_j(z)}$$
$$= \lim_{z \to z_j} \tilde{c}_k(z)/\tilde{c}_j(z) = \delta_{jk}$$

and $g(z_j) = \lim_{z \to z_j} \sum_{k=1}^{n} c_k(z)\hat{z}_k = \hat{z}_j$, as required. $\square$

Note that the statement of the theorem also holds if $\gamma_k r_j$ for $k = j-1, j$ is discontinuous at z_j, as long as the limit exists and is finite for any direction in which z approaches z_j, that is, $\lim_{t \to 0^+} |(\gamma_k r_j)(z_j + t\zeta)| < \infty$ for any $\zeta \in \mathbb{C}$.

Let us now turn to a similar set of sufficient conditions that guarantee the interpolation of the target edges.

Theorem 6 Let $\eta_j(t) = (1-t)z_j + t z_{j+1}$ with $t \in (0,1)$ be a point on the (open) source edge (z_j, z_{j+1}) and let $\hat{\eta}_j(t)$ be its image under s_j,

$$\hat{\eta}_j(t) = s_j(\eta_j(t)) = (1-t)\hat{z}_j + t\hat{z}_{j+1}.$$

The complex barycentric mapping g in (14) interpolates the j-th (open) target edge, if

$$\lim_{z \to \eta_j(t)} |\gamma_j(z)| = \infty \quad \text{and} \quad \lim_{z \to \eta_j(t)} |\gamma_k(z)| < \infty, \quad k \neq j$$

for all $t \in (0,1)$.

Proof A similar reasoning as in the proof of Theorem 5 shows that $\lim_{z \to \eta_j} \gamma_k(z)/\gamma_j(z) = \delta_{jk}$, hence

$$
\begin{aligned}
g(\eta_j) &= \lim_{z \to \eta_j} \sum_{k=1}^{n} \gamma_k(z) s_k(z) \bigg/ \sum_{k=1}^{n} \gamma_k(z) \\
&= \lim_{z \to \eta_j} \sum_{k=1}^{n} \big(\gamma_k(z)/\gamma_j(z)\big) s_k(z) \bigg/ \sum_{k=1}^{n} \big(\gamma_k(z)/\gamma_j(z)\big) \\
&= \lim_{z \to \eta_j} s_j(z) = s_j(\eta_j),
\end{aligned}
$$

as required. $\square$

4. Designing new complex barycentric mappings

We now use our insight into the structure of complex barycentric mappings from the previous sections to derive some recipes for synthesizing new types of these mappings having desirable properties.

4.1. Primal/dual vertices

Several authors [JSWD05, LBS06, SJW07] have shown that three-point real-valued coordinates can also be expressed as *dual/primal* ratios involving the *primal* edge r_j and a *dual* edge d_j between two dual vertices, $d_j = w_j - w_{j-1}$ (there is one dual vertex w_j per triangle $[z, z_j, z_{j+1}]$ in Figure 2), when considered as complex numbers,

$$
\tilde{c}_j = i \frac{d_j}{r_j}. \tag{15}
$$

Since r_j and d_j are always orthogonal for the three-point coordinates, this ratio is pure real. Combining (10) and (15) yields the following general relationship between w_j and γ_j,

$$
\gamma_j = i w_j \frac{e_j}{r_j r_{j+1}} \quad \Longleftrightarrow \quad w_j = -i \gamma_j \frac{r_j r_{j+1}}{e_j}. \tag{16}
$$

Note that there is a single (translational) degree of freedom in choosing the w_j's, which corresponds exactly to the degree of freedom described by (11) in choosing γ_j. This general expression for γ_j makes sense since the weight of the similarity s_j should be proportional to the length of e_j (a longer edge has larger influence) and inversely proportional to the distances of z from z_j and z_{j+1}, that is, to the lengths of r_j and r_{j+1}.

The barycentric mapping is thus determined by the dual vertices w_j which "represent" the triangles $[z, z_j, z_{j+1}]$. It is well known that for the discrete harmonic coordinates, w_j is the circumcenter of $[z, z_j, z_{j+1}]$, which is a vertex of the Voronoi cell of the site z. A generalized version of these coordinates may be obtained by resorting to the *generalized* Voronoi diagram (also known as a *power* diagram) [MMdGD11]. For this, a disc D_j of radius R_j is centered at each vertex z_j, and w_j is then the circumcenter of the triangle $[z, y_j, y_{j+1}]$, where $y_j = z_j - R_j \frac{r_j}{|r_j|}$ is the intersection of D_j and the ray from z_j through z. The simple Voronoi cell is just the special case where all $R_j = 0$. Note that even in the general case the coordinates in (15) are pure real.

4.2. Holomorphic vertex-interpolating mapping

As Mercat [Mer08] points out, *complex* dual/primal ratios arise in (15) when the primal and dual edges are not orthogonal. An interesting example is obtained by taking the dual vertex of $[z, z_j, z_{j+1}]$ to be its barycentre $(z + z_j + z_{j+1})/3$, or equivalently, after translating everything by $-z$, to be $w_j = (r_j + r_{j+1})/3$. Applying (16) and dividing by $i/3$ yields

$$
\gamma_j = \frac{r_{j+1}}{r_j} - \frac{r_j}{r_{j+1}}. \tag{17}
$$

Since these γ_j are holomorphic, the result is a holomorphic map that interpolates the vertices (but not the edges), according to Theorem 5 and as shown in Figures 1 (c) and 3 (c). As

$$
\begin{aligned}
\mathrm{Im}(\Gamma) &= \sum_{j=1}^{n} \mathrm{Im}\left(\frac{r_{j+1}}{r_j}\right) - \sum_{j=1}^{n} \mathrm{Im}\left(\frac{r_j}{r_{j+1}}\right) \\
&= \sum_{j=1}^{n} \frac{\mathrm{Im}(r_{j+1}\bar{r}_j)}{|r_j|^2} - \sum_{j=1}^{n} \frac{\mathrm{Im}(r_j\bar{r}_{j+1})}{|r_{j+1}|^2} \\
&= 2 \sum_{j=1}^{n} A_j \left(\frac{1}{|r_j|^2} + \frac{1}{|r_{j+1}|^2}\right),
\end{aligned}
$$

we conclude that $\Gamma(z) \neq 0$ if z lies in the kernel of Ω, hence the holomorphic barycentric mapping with weights in (17) is guaranteed to be well-defined for any convex source polygon. But it is possible to create examples with non-convex Ω and $\Gamma(z) = 0$ for some $z \in \Omega$.

4.3. Non-holomorphic interpolating mappings

All the complex mappings presented so far were either holomorphic or real-valued. Using Theorems 5 and 6 we can design non-holomorphic mappings, which are not real-valued, yet interpolate the target polygon. Our primary goal is not to advocate the use of these specific mappings, but rather to demonstrate how to design "tailor-made" coordinates with desirable properties.

The common starting point for many real-valued coordinates are the weight functions $1/|r_j|$, as the most basic requirement is that the influence of a vertex decays as the distance to that vertex increases. To fulfill the requirements of Theorem 5, we start off with $\gamma_j^v = 1/|r_j r_{j+1}|$, so that γ_j^v grows to infinity as z approaches either endpoint of the edge $[z_j, z_{j+1}]$. As we additionally require interpolation on the edges, we define $\gamma_j^e = 1/(\pi - \theta_j)$, where $\theta_j(z)$ is the *signed* angle of the triangle $[z, z_j, z_{j+1}]$ at z (see Figure 2). Since $\theta_j(z)$ converges to π as z approaches any point on the open edge (z_j, z_{j+1}) from inside Ω, this γ_j^e satisfies the conditions of Theorem 6. Finally, we combine these two quantities, multiply them with the factor $|e_j|$ to give larger weights to longer edges, and obtain the *Made-to-order Angle Guided Interpolating Coordinates* (or simply *MAGIC*)

$$
\gamma_j = |e_j| \gamma_j^v \gamma_j^e = \left| \frac{e_j}{r_j r_{j+1}} \right| \frac{1}{\pi - \mathrm{Im}(\log(r_{j+1}/r_j))}, \tag{18}
$$

where we used the fact that $\theta_j = \mathrm{Im}(\log(r_{j+1}/r_j))$.
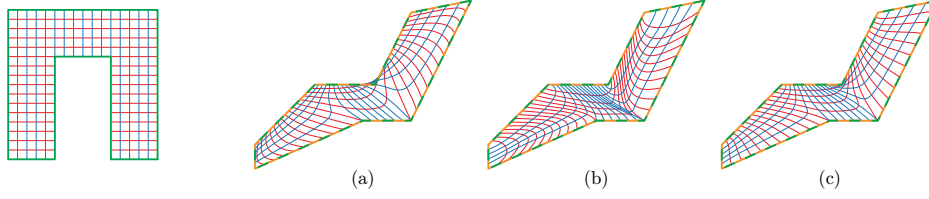
Figure 4: *Comparison of the real-valued mean value mapping (a), our complex MAGIC mapping (b), and their average (c).*

These coordinates have some interesting properties. First, it is clear that all $\gamma_j(z)$ are positive for any z not on the boundary of Ω, because $\theta_j(z) \in (-\pi, \pi)$. Therefore, their sum $\Gamma(z)$ is also positive and the coordinates are well-defined. Second, it is not too hard to show that the γ_j in (18) satisfy the conditions of Theorems 5 and 6, hence the resulting barycentric mapping interpolates the target polygon. However, we should note that $\theta_j(z)$ converges to $-\pi$ as z approaches the open edge (z_j, z_{j+1}) from outside Ω, hence neither θ_j nor γ_j are continuous across the edge $[z_j, z_{j+1}]$. As a consequence, MAGIC mappings should be used for the interior of Ω only.

Figure 4 shows a comparison between mean value and MAGIC mappings for a non-convex source polygon. We observe that vertices that are reflex (concave) in the source polygon tend to repel in mean value mappings, whereas these vertices act as attractors in MAGIC mappings. A possible explanation is that mean value coordinates divide by the signed area of the triangle $[z, z_j, z_{j+1}]$, yielding negative weights in concave regions. In contrast, MAGIC weights are always positive.

We found that it is often beneficial to mediate between both effects and that a simple average of mean value and MAGIC mappings (i.e., averaging the respective γ_j weights) yields very pleasing deformations as shown in Figure 4 (c). The resulting mapping is well-defined because $\Gamma(z)$ is positive both for MAGIC and for mean value coordinates [HF06], hence it is also positive for any convex combination of the two.

4.4. Polynomial edge-to-edge mappings

In Section 3 we derived the normal form (14) of complex barycentric mappings as a blend of edge-to-edge mappings. A natural extension of this construction seems to be the generalization of these *linear* mappings s_j to higher-order *polynomial* mappings, hence changing the "speed" along the target edge $[\hat{z}_j, \hat{z}_{j+1}]$, while maintaining interpolation along the edge. That is, we replace s_j by a mapping $\tilde{s}_j$ that satisfies

$$\tilde{s}_j((1-t)z_j + tz_{j+1}) = (1-\sigma_j(t))\hat{z}_j + \sigma_j(t)\hat{z}_{j+1} \quad (19)$$

for $t \in [0, 1]$, where $\sigma_j : \mathbb{R} \to \mathbb{R}$ is a polynomial speed function of some degree $d \geq 1$ with $\sigma_j(0) = 0$ and $\sigma_j(1) = 1$. Moreover, σ_j should be monotonic on the interval $[0, 1]$, in order to maintain bijectivity along the edge.

The simplest way to design such a mapping $\tilde{s}_j$ is to interpret σ_j as a complex polynomial and let

$$\tilde{s}_j = \hat{z}_j + (\hat{z}_{j+1} - \hat{z}_j)\sigma_j(-r_j/e_j). \quad (20)$$

This choice of $\tilde{s}_j$ clearly satisfies condition (19), because any point $z = ((1-t)z_j + tz_{j+1})$ on the edge $[z_j, z_{j+1}]$ satisfies

$$r_j(z) = z_j - z = z_j - (1-t)z_j - tz_{j+1} = -te_j, \quad (21)$$

and it has the advantage of being holomorphic, so that blending these $\tilde{s}_j$ with holomorphic weight functions γ_j guarantees that the resulting barycentric mapping

$$\tilde{g}(z) = \sum_{j=1}^{n} \gamma_j(z)\tilde{s}_j(z) \Big/ \sum_{j=1}^{n} \gamma_j(z)$$

is also holomorphic.

The idea of quadratic speed functions along the edges also appeared in the construction of generalized Cauchy coordinates by Weber and Gotsman [WG10, Section 5.2], but in a slightly different way. If we use, on the one hand, quadratic speed functions $\sigma_j(t) = t + 4\alpha_j(1-t)t$ and the Cauchy–Green weight functions $\gamma_j = \log(r_{j+1}/r_j)$ in our approach, and on the other hand the images of the source edge midpoints,

$$\hat{z}_j^c = \tilde{s}_j((z_j + z_{j+1})/2) = (1/2 - \alpha_j)\hat{z}_j + (1/2 + \alpha_j)\hat{z}_{j+1},$$

as the additional constraints in the continuous case of generalized Cauchy coordinates, then the two resulting mappings differ only by the term

$$\sum_{j=1}^{n} \frac{\alpha_j}{\pi i}(\hat{z}_j + \hat{z}_{j+1}) - \sum_{j=1}^{n} \frac{2\alpha_j}{\pi i}s_j. \quad (22)$$

The derivation of this result is simple but rather lengthy and omitted here. A comparison of the two mappings is shown in Figure 5 (a,b). Both mappings do not really pick up the prescribed speed along the boundary very well. For our weighted quadratic edge-to-edge mappings (b), the three constraints (in this example, $\alpha_j \neq 0$ for the top horizontal and the two leftmost vertical edges) even have an undesirable global shifting effect, which is explained mainly by the first term in (22); whereas the second term in (22) explains the slight shape difference of the two results.

One intrinsic problem of using quadratic speed functions σ is that they are not bijective on $\mathbb{R}$, and so the resulting quadratic edge-to-edge mapping $\tilde{s}$ folds back onto itself,
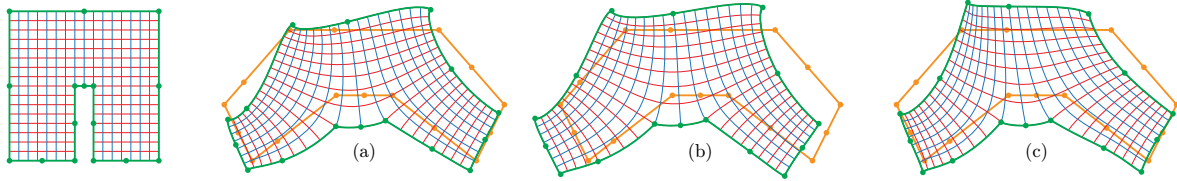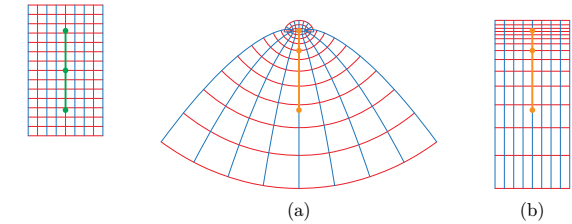
Figure 5: *Comparison of the complex barycentric mappings based on continuous generalized Cauchy coordinates (a), weighted holomorphic (b) and non-holomorphic (c) quadratic edge-to-edge mappings.*
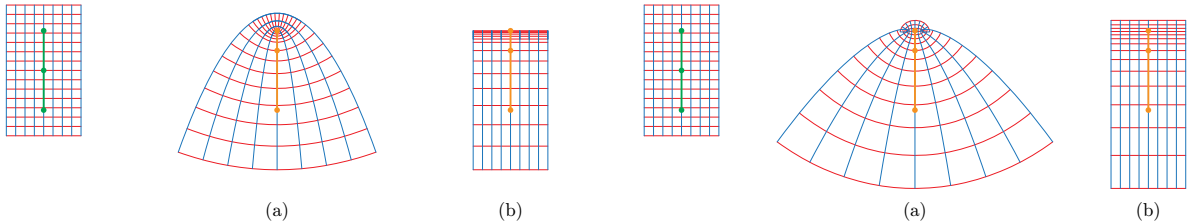
Figure 6: *Holomorphic (a) and non-holomorphic (b) edge-to-edge mapping $\tilde{s}$ for the speed function $\sigma(t) = t^2$ (edge direction is from top to bottom).*

Figure 7: *Holomorphic (a) and non-holomorphic (b) edge-to-edge mapping $\tilde{s}$ for the speed function $\sigma(t) = (t + 2t^3)/3$ (edge direction is from top to bottom).*

even along the line L defined by the target edge as illustrated in Figure 6 (a). This problem can be resolved by resorting to globally monotonic speed functions with odd degree d. But although they guarantee $\tilde{s}$ to be bijective on L, global bijectivity cannot be achieved this way. Often the singularities of $\tilde{s}$ appear rather close to the target edge, as shown in Figure 7 (a), which in turn can have undesirable effects on the overall barycentric mapping.

To overcome the latter problem, another option is to extend the polynomial behaviour along the edge orthogonally into the complex plane and let

$$\tilde{s}_j = \hat{z}_j + (\hat{z}_{j+1} - \hat{z}_j)\left[\sigma_j\big(\text{Re}(-r_j/e_j)\big) + \text{Im}(-r_j/e_j)i\right].$$

Again, it follows from (21) that these $\tilde{s}_j$ satisfy (19). In contrast to the choice in (20), these edge-to-edge mappings are not holomorphic, but they have the advantage of being bijective as long as σ_j is bijective; see Figures 6 (b) and 7 (b). Using these non-holomorphic edge-to-edge mappings in the example above, we observe in Figure 5 (c) that the resulting barycentric mapping does a much better job in picking up the prescribed boundary behaviour, at the price of not being holomorphic.

In general, the extra degrees of freedom in the overall complex barycentric mapping that we gain by considering polynomial instead of linear edge-to-edge mappings may be used to improve the quality of the mapping, for example, to make it more conformal or bijective. We implemented an interactive tool where the user controls each polynomial mapping $\tilde{s}_j$ by specifying the images of $d-1$ uniformly distributed points from the source edge $[z_j, z_{j+1}]$ on the target

edge $[\hat{z}_j, \hat{z}_{j+1}]$. Figure 8 shows an example with the mean value weights from (13). For linear s_j, the mapping is the classical mean value mapping and not bijective in this case. However, the mapping can be made bijective by using cubic $\tilde{s}_j$ from (20) to decrease the interpolation speed around the concave target vertex and the vertex diagonally across. Whether or not this is possible for any source and target polygon is an interesting question for future research.

5. Conclusion

Complex barycentric mappings provide a flexible tool for designing planar deformations. They are appealing for interactive applications like image deformation because of two reasons. On the one hand, they can be evaluated efficiently by the formulas (8) or (14), on the other hand it is relatively easy to realize a variety of properties, including interpolation constraints and angle-preservation.
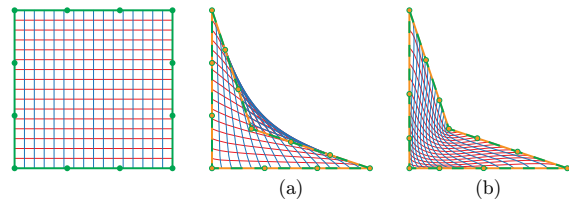
Figure 8: *Comparison of the classical mean value mapping (a), which interpolates edges linearly, and a modified complex version based on cubic edge-to-edge mappings (with the same mean value γ_j) (b).*

One key insight of our research is that the edge-based normal form (14) has a number of advantages over the classical vertex-based form (8). First, it automatically takes care of the affine precision property. Second, we show in Theorem 1 that barycentric mappings based on classical real-valued coordinates can easily be expressed in the complex form (14). This allows one to consider blends between them and other purely complex barycentric mappings, which in turn can improve the quality of the mapping significantly as shown in Figure 4 (c). Third, both vertex and edge interpolation constraints can easily be modelled into the weight functions γ_j by respecting the sufficient conditions in Theorems 5 and 6, as shown in Sections 4.2 and 4.3. Finally, the normal form (14) opens up the way to further generalize complex barycentric mappings by modifying the edge-to-edge mappings s_j as demonstrated in Section 4.4. This new flexibility can be used to create bijective interpolating mappings, which so far could be achieved only with Wachspress mappings between convex source and target polygons [FK10].

So far, we explored the advantages of blending polynomial edge-to-edge mappings only interactively, but we believe that the full potential of this approach will crop up when the additional degrees of freedom are determined by minimizing an appropriate energy that measures the overall conformality or bijectivity of the mapping. Another interesting direction that we consider worth exploring is the connection of this approach to moving least squares coordinates [MS10], which are similar in spirit, as they also allow for polynomial behaviour along the edges.

Acknowledgements

References

[EDD*95] ECK M., DEROSE T., DUCHAMP T., HOPPE H., LOUNSBERY M., STUETZLE W.: Multiresolution analysis of arbitrary meshes. In *Proceedings of SIGGRAPH* (Los Angeles, Aug. 1995), pp. 173–182. 2

[FHK06] FLOATER M. S., HORMANN K., KÓS G.: A general construction of barycentric coordinates over convex polygons. *Advances in Computational Mathematics 24*, 1–4 (Jan. 2006), 311–331. 2, 3

[FK10] FLOATER M. S., KOSINKA J.: On the injectivity of Wachspress and mean value mappings between convex polygons. *Advances in Computational Mathematics 32*, 2 (Feb. 2010), 163–174. 10

[Flo03] FLOATER M. S.: Mean value coordinates. *Computer Aided Geometric Design 20*, 1 (Mar. 2003), 19–27. 2

[HF06] HORMANN K., FLOATER M. S.: Mean value coordinates for arbitrary planar polygons. *ACM Transactions on Graphics 25*, 4 (Oct. 2006), 1424–1441. 2, 8

[HS08] HORMANN K., SUKUMAR N.: Maximum entropy coordinates for arbitrary polytopes. *Computer Graphics Forum 27*, 5 (July 2008), 1513–1520. Proceedings of SGP. 2

[JLW07] JU T., LIEPA P., WARREN J.: A general geometric construction of coordinates in a convex simplicial polytope. *Computer Aided Geometric Design 24*, 3 (Apr. 2007), 161–178. 2

[JMD*07] JOSHI P., MEYER M., DEROSE T., GREEN B., SANOCKI T.: Harmonic coordinates for character articulation. *ACM Transactions on Graphics 26*, 3 (July 2007), Article 71, 9 pages. Proceedings of SIGGRAPH. 2

[JSWD05] JU T., SCHAEFER S., WARREN J., DESBRUN M.: A geometric construction of coordinates for convex polyhedra using polar duals. In *Proceedings of the Third Symposium on Geometry Processing* (Wien, July 2005), pp. 181–186. 7

[LBS06] LANGER T., BELYAEV A., SEIDEL H.-P.: Spherical barycentric coordinates. In *Proceedings of the Fourth Symposium on Geometry Processing* (Cagliari, June 2006), pp. 81–88. 7

[LKCOL07] LIPMAN Y., KOPF J., COHEN-OR D., LEVIN D.: GPU-assisted positive mean value coordinates for mesh deformations. In *Proceedings of the Fifth Symposium on Geometry Processing* (Barcelona, July 2007), pp. 117–123. 2

[LLCO08] LIPMAN Y., LEVIN D., COHEN-OR D.: Green coordinates. *ACM Transactions on Graphics 27*, 3 (Aug. 2008), Article 78, 10 pages. Proceedings of SIGGRAPH. 2

[Mer08] MERCAT C.: Discrete complex structure on surfel surfaces. In *Discrete Geometry for Computer Imagery*, Coeurjolly D., Sivignon I., Tougne L., Dupont F., (Eds.), vol. 4992 of *Lecture Notes in Computer Science*. Springer, 2008, pp. 153–164. 7

[MLBD02] MEYER M., LEE H., BARR A., DESBRUN M.: Generalized barycentric coordinates on irregular polygons. *Journal of Graphics Tools 7*, 1 (2002), 13–22. 2

[MMdGD11] MULLEN P., MEMARI P., DE GOES F., DESBRUN M.: HOT: Hodge-optimized triangulations. *ACM Transactions on Graphics 30*, 4 (Aug. 2011). Proceedings of SIGGRAPH. 7

[MS10] MANSON J., SCHAEFER S.: Moving least squares coordinates. *Computer Graphics Forum 29*, 5 (July 2010), 1517–1524. Proceedings of SGP. 10

[PP93] PINKALL U., POLTHIER K.: Computing discrete minimal surfaces and their conjugates. *Experimental Mathematics 2*, 1 (1993), 15–36. 2

[SJW07] SCHAEFER S., JU T., WARREN J.: A unified, integral construction for coordinates over closed curves. *Computer Aided Geometric Design 24*, 8–9 (Nov.–Dec. 2007), 481–493. 7

[Wac75] WACHSPRESS E. L.: *A Rational Finite Element Basis*, vol. 114 of *Mathematics in Science and Engineering*. Academic Press, New York, 1975. 2

[WBCG09] WEBER O., BEN-CHEN M., GOTSMAN C.: Complex barycentric coordinates with applications to planar shape deformation. *Computer Graphics Forum 28*, 2 (Apr. 2009), 587–597. Proceedings of Eurographics. 2, 3, 6

[WG10] WEBER O., GOTSMAN C.: Controllable conformal maps for shape deformation and interpolation. *ACM Transactions on Graphics 29*, 4 (July 2010), Article 78, 11 pages. Proceedings of SIGGRAPH. 6, 8

[ZS08] ZILL D., SHANAHAN P.: *A First Course in Complex Analysis With Applications*. Jones and Bartlett Publishers, 2008. 6